Contents lists available at ScienceDirect

Food Chemistry: X

A two-dimensional correlation spectroscopy analysis-based approach for asymptomatic rot detection in stored potatoes using hyperspectral imaging

Fan Zhang [1], Wenxiu Wang [1], Qianyun Ma, Qi Shi, Kexiang Chen, Xinyue Pan, Shiyuan Xie, Jianfeng Sun [*]

College of Food Science and Technology, Hebei Agricultural University, 289th Lingyusi Street, Lianchi District, Baoding 071000, China.

ARTICLE INFO

ABSTRACT

Fusarium dry rot (FDR), which is caused by several Fusarium species, is a major disease affecting potatoes during storage. The study aimed to identify the gleyic stage and monitor rot progression in stored potatoes using a hyperspectral imaging (HSI) system. We evaluated the susceptibility parameters and quality attributes during the infection process and monitored starch, soluble protein, malondialdehyde, and aerobic bacterial contents in all samples. To further characterize the infection process, we collected spectral data on different storage days and then mapped these data using two-dimensional correlation spectroscopy. The results revealed 20 peaks related to these component contents. Then, the quantitative analysis models of these indicators were established based on the 2D correlation synchronization spectrum. The optimal correlation coefficients of the validation set were 0.9273, 0.9634, 0.9470, and 0.9487 for these indicators. Visual analysis was implemented to these indicators, and the content distribution can be effectively observed on hyperspectral images.

1. Introduction

Potatoes rank as the fourth largest crop worldwide after rice, wheat, and maize. They are highly adaptable, produce high yields, and are widely cultivated, making them a good source of dietary carbohydrates, vitamins, and minerals (Singh & Saldaña, 2011; Wood & Carragher, 2017). However, potatoes are susceptible to various diseases before and during postharvest storage, leading to enormous economic losses and posing a substantial threat to global food safety (Macauley, 1982; Veltman et al., 2023). Dry rot disease is one of the most common fungal diseases caused by infestation with different *Fusarium* species during storage. After *Fusarium* infection, potatoes enter the gleyic stage, during which they show no surface symptoms despite infection. Following the gleyic stage, fungal spores infiltrate the potato surface and continuously reproduce, and the disease shifts from a recessive to a dominant state, eventually leading to the development of both external and internal potato lesions. Consequently, these biotic stresses severely affect the nutritional and quality properties of tubers (Ren et al., 2021). Therefore, effective identification of the gleyic stage was crucial.

Traditional methods for detecting potato dry rot disease mainly involve manual detection, which relies on the subjective judgment of an inspector. Visual diagnosis is usually based on the appearance of brown or black spots on the potato surface and associated pile shrinkage. However, manual detection methods are time-consuming, labor-intensive, time-lagged, and do not meet the current demand for disease detection. Additionally, although polymerase chain reaction analysis has shown greater accuracy in detecting the disease, it requires expertise and equipment for accurate results detection and interpretation. Recently, computer vision technology has been employed in the non-destructive detection of disease; however, it cannot identify the gleyic stage. Therefore, to ensure the safety of potatoes, developing an accurate, rapid, non-destructive, real-time, and stable method is necessary to achieve the earliest possible diagnosis of dry rot disease.

Besides, the obtained hyperspectral images usually have high-dimensional data and contain a lot of redundant information, which reduces computational efficiency and model performance. To solve the problem, characteristic wavelength selection is usually used to select information variables, excluding information variables and noise variables, while ensuring a short computational modeling time. Some methods for selecting characteristic wavelengths include the competitive adaptive reweighted sampling algorithm (CARS), genetic algorithm (GA), and successive algorithm (SPA), which are widely used in existing

research. These algorithms select feature wavelengths based on the accuracy of predictions from a statistical perspective and achieve good prediction accuracy. They can select a combination of key features with great competence. However, from the standpoint of interpretability, the variables chosen to represent the functional group or property of interest of the analyte are poorly interpreted (Yun et al., 2019; Zhao et al., 2020). Based on this, the 2D-COS algorithm was employed in this study to screen the feature wavelengths for potato dry-rot-related quality attributes. 2D-COS can directly reflect the correlation between the spectra and external disturbance variables. In contrast to traditional one-dimensional (1D) spectroscopy, 2DCOS can improve spectral resolution by extending the original data into two dimensions and emphasizing features that are not easily observed in one-dimensional spectra (Ding et al., 2021). From the 2D correlation spectra, we can distinguish the overlap and weak absorption peak changes in the original spectra, including the absorption peak displacement and the absorption peak intensity changes under the action of disturbance. Previous studies have applied 2D-COS to detect rice adulteration (An et al., 2024; Wu et al., 2020) and pear disease (Zhang et al., 2022), providing evidence that 2D-COS can directly reflect the correlation between spectra and external disturbance variables. Thus, we believe that this approach holds potential for applications in the analysis of the typical physicochemical indexes in potatoes during the process of fungal infection and may facilitate the identification of the gleyic stage of potato dry rot.

In general, the purpose of this study was to monitoring changes in some quality parameters during fungal infection, and determine a quantitative model to detect asymptomatic potatoes with dry rot disease. The specific purpose is as follows: (1) Monitoring the variations of starch, soluble proteins, MDA and aerobic bacterial counts in the course of infection. (2) Combining hyperspectral imaging with 2D-COS and CARS algorithms to identify characteristic wavelengths related to fungal infections. (3) Establishing least squares vector machine (LS-SVM) and partial least squares regression (PLSR) models for quantitative analysis of quality attributes about potato dry rot disease. (4) Visually present starch, MDA, and soluble protein distributions, as well as aerobic bacterial counts in potato samples. In this study, an efficient method was expected to be developed to interpret HSI spectra of diseased potatoes and identify the most effective variables in a rapid and accurate manner.

2. Materials and methods

2.1. Sample preparation

Fresh potato samples at commercial maturity were purchased from a local market in Baoding and immediately transported to Hebei Agricultural University, where they were stored at 4 °C. A total of 149 fresh potatoes with similar maturity, size, and quality (without apparent defects, physical injuries, or disease infection) were selected and washed in a 3% (v/v) sodium hypochlorite solution for 8 min, rinsed with distilled water, and then air-dried. The function of 3% (v/v) sodium hypochlorite solution was to disinfect and sterilize the samples. Before the sample was inoculated with fungal suspension, it is necessary to ensure that the surface of the sample is sterile to avoid other fungal infections at a later stage. Six naturally infected potatoes were collected to isolate the pathogens involved and cultured on potato dextrose agar (PDA) medium at 25 °C for 8 d to induce sporulation. Fungal spores were washed in 50 mL Falcon tubes using approximately 20 mL of distilled water containing 0.05% (v/v) Tween-80. After intense mixing, each solution was gravity-filtered through double-layered 20 μm nylon mesh into a 50 mL Falcon tube to separate the spores from mycelial debris and PDA medium, and the spore concentrations in the filtrates were adjusted to approximately 106 spores·mL-1 using a hemocytometer. Potatoes were injected in three areas on their surfaces with 10 μL of a Fusarium elderberry spore suspension. The inoculated samples were stored in an artificial climate chamber to maintain them at a relative humidity of 90% and a temperature of 25 °C. To obtain potato samples with different degrees of corruption, six samples were inoculated every day, and the whole experiment lasted for 21 d. Then, 126 potato samples with different degrees of corruption and 23 samples from healthy (untreated) potatoes were acquired for subsequent experiments.

As shown in Table 1, all samples were divided into four categories according to the classification standard of potato dry rot. The samples were classified in terms of their degrees of corruption, namely 23 healthy samples, 18 asymptomatic samples (D1), 91 mild corruption samples (D2), and 17 severe corruption samples (D3).

2.2. HSI system

The specially designed HSI system consists of a 12-bit charge-coupled device camera (Sensicam QE, The Cooke Incorporation, Germany), an imaging spectrometer (Imspector V10E, Spectral Imaging, Ltd., Finland), a lens with a focal length of 12.7 mm, a 10–250 W adjustable halogen tungsten lamp, a customized linear optical fiber beam, a two-dimensional translation platform, and a computer. Hyperspectral images of potato samples were collected at a wave bandwidth of 920–2086 nm. The size of a hyperspectral image of one potato ranged from 1900 to 1024 to 2200–1024 pixels for 209 bands. To minimize the influence of interference light, the components were fixed in a cabinet without light. To remove the noise caused by equipment and environmental interference, we performed black-and-white correction for the original hyperspectral image ($R_{orignal}$). The correction process required a black image (R_{dark}) with a reflectance close to 0% (obtained using a black lens cover over the lens) and a white image (R_{white}) with a reflectance close to 100% (obtained using a uniform whiteboard made of tetrafluoroethylene). The following equation was used to correct images by a white and dark references, where R is the corrected image.

$$R = \frac{R_{orignal} - R_{dark}}{R_{white} - R_{dark}}$$

2.3. Physiological and biochemical indicators determination

Samples were collected from 0 to 21 days, and three tissues were collected from each potato sample, and the sampling location was the junction of disease and health of potato tuber. The samples were frozen in liquid nitrogen and stored in the refrigerator at −80 °C. All indicators were determined by 5 g potato samples.

2.3.1. Starch content measurement

Starch content was measured using Starch Assay Kit (Cat#BC0700) from Solarbio Life Sciences (Beijing, China) following the manufacturer's protocols. The content of starch is obtained by the following formula:

$$S \, (\text{mg/g FW}) = x \times C \times (V/W)$$

where S is the starch content, x is the starch concentration obtained using the standard curve, C is the dilution multiple, V is the extracted volume (1.7 mL), and W is the fresh weight of the sample in g.

2.3.2. MDA content measurement

MDA content was measured using MDA Content Assay Kits (Cat#BC0020) from Solarbio Life Sciences (Beijing, China) following the manufacturer's protocols. The MDA contents were obtained with the

Table 1
Criteria used to classify potatoes as having dry rot disease.

Degree	Standard
Healthy	Uninoculated samples
D 1	Potato samples without disease spots
D 2	Potatoes with spot areas totaling <5% of the surface area
D 3	Potatoes with spot areas totaling <15% of the surface area

following formula:

$$MDA\ (mmol/kg\ FW) = \left(\Delta A \times V_1/[\varepsilon \times d] \times 10^3\right)/\left(W \times [V_2/V_3]\right)$$
$$= 25.8 \times \Delta A/W$$

where ΔA is the absorbance at 532 nm minus the absorbance at 600 nm, V_1 is the total volume of the reaction system, ε is the molar extinction coefficient of MDA (155×103), d is the optical diameter of the colorimetric dish (1 cm), W is the sample weight (kg), V_2 is the volume of sample added (0.2 mL), and V_3 is the volume of extraction liquid added (1 mL).

2.3.3. Soluble protein content measurement

Soluble protein contents were determined by Coomassie bright blue G-250 staining (Zheng et al., 2018). For each sample, 0.05 g potato was ground in a mortar, and 3 mL of phosphate-buffered solution was added. The extract was centrifuged at 13,000 $\times g$ for 15 min at 4 °C, and 0.1 mL of the resulting supernatant was combined with 4.9 mL Coomassie brilliant blue G-250 solution. After 2 min, the soluble protein content of each sample was determined at 595 nm using an ultraviolet spectrophotometer.

2.3.4. Aerobic bacterial counts measurement

The aerobic bacterial count was determined using a Chinese national food safety standard (GB/T 4789.2–2016; Food microbiological

examination - Aerobic plate count), Each sample was tested three times, and the average values were calculated as the final value.

2.4. Hyperspectral data processing

We used MATLAB R2014b and ENVI 15.1 software to implement all models and data processing. As shown in Fig. 1, our HSI analysis included the following main steps: (a) collecting raw images of potatoes, (b) hyperspectral image acquisition and calibration, (c) extracting the region of interest (ROI) and spectral data, (d) and spectral analysis involving data pretreatment and feature band selection based on the 2D-COS and CARS algorithm. Subsequently, models were established to predict the components of the potato samples (starch, MDA, soluble protein, and aerobic bacterial counts).

2.5. ROI extractions

We used ENVI software to extract spectral data from the hyperspectral images. In addition to characteristic spectra, the original hyperspectral image contained background, noise and other spectra that do not represent the key potato sample information required. Therefore, these unusable spectra were filtered out to extract the ROI.

Considering an entire potato area as the ROI using the threshold method, as shown in Fig. 1. The ROI was identified based on differences in gray shading between the specific target and the image background.
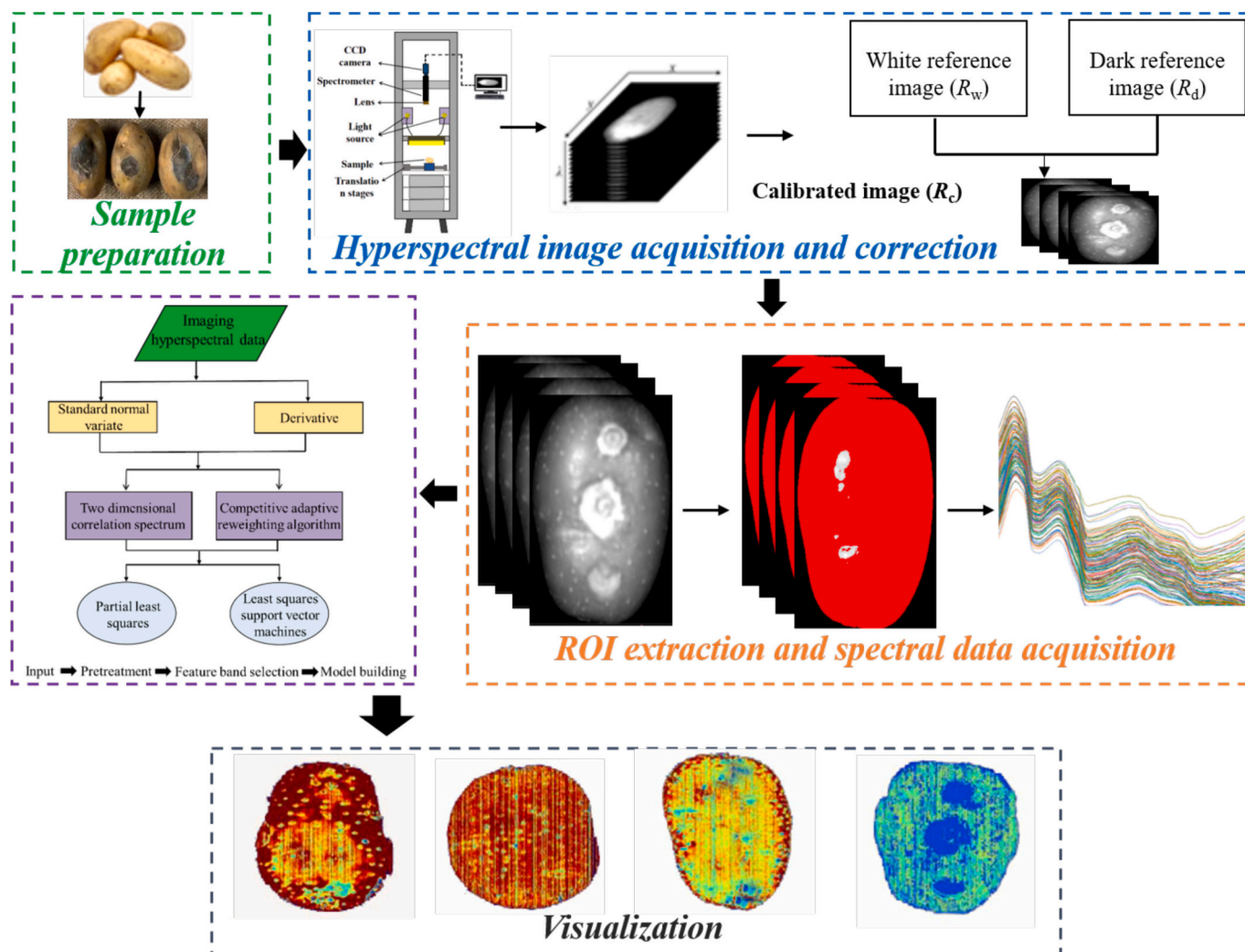

Fig. 1. Test and data processing flow chart.

The pixel levels were divided into several categories by setting the threshold value to effectively separate the target from the background. We determined whether the image pixels belonged to the target or the background area by adjudicating whether the characteristic attributes of each pixel in the image meet the requirements of the threshold value. Subsequently, each gray image was converted to a binary image. Determining an optimal threshold was crucial, and this was achieved based on the relationship between the peaks and troughs of the sample image histograms.

2.6. Spectral pretreatments

It is typically necessary to preprocess raw hyperspectral data before conducting multivariate calibration because the measured spectra of complex samples are frequently affected by the image background, light scattering, varying degrees of noise, and other unexpected disturbances (Bian et al., 2020; Zhang et al., 2019). We processed the original spectral data by performing (i) smoothing treatments, (ii) First derivative (FD) treatments, (iii) second derivative (SD) treatments, (iv) standard normal variate transformation (SNV) treatments, and (v) combinations thereof analyzed in different orders. The spectral pretreatments were conducted using PLS Toolbox software (version 7.5).

2.7. Feature bands selection

2.7.1. 2D-COS analysis

2D-COS can be used to effectively improve the spectral resolution and resolve overlapping spectral bands by designing perturbations (Dong, Zhang, et al., 2021; Dong, Zuo, et al., 2021; Sui et al., 2014) and offers two key advantages, namely, high resolution and flexible timing rules. When obtaining spectral measurements, some external disturbances (such as the temperature and concentration) can cause changes in the compositional structure of the system and background environment. These changes, in turn, can cause change in the measured spectra. For example, the spectral changes triggered by external disturbances result in a dynamic spectrum, and two-dimensional correlation calculations of dynamic spectra can be used for 2D-COS analysis. Among these two-dimensional correlations, the synchronous correlation spectrum is calculated as follows:

$$\varnothing = \frac{1}{S-1} \, MM^T$$

and the asynchronous correlation is calculated as follows:

$$\psi = \frac{1}{S-1} \, MHM^T$$

where M is the spectral matrix composed of some wavelengths and S samples, and H represents the Hilbert transformation matrix. 2D-COS was conducted using 2D-COS software, which is freely available on a website created by Tao Zhou (httop://muchong.com/t-9696009-1).

In addition, 2D-COS analysis was performed in the present study to identify changes occurring in the chemical composition of dry rot potatoes during infection. The infection days were used as the external disturbance; the minimum storage time was 0 d and the maximum storage time was 21 d. Between the minimum and maximum storage time, the step length was 1 d, a total of 21 steps; as a result, the dimensions of matrix X were 21 × 209. We selected the 920–2086 nm spectral region of each sample to calculate its 2D correlation spectrum. First, OMNIC software was used for automatic baseline correction of all spectra, which accurately reflects the band changes in 1D spectra and renders the automatic peaks more pronounced. Second, 1D spectra were divided into different regions to improve the definition of spectral peaks, and synchronous and asynchronous 2D-COS correlation spectra were calculated based on the discrete Hilbert transform algorithm.

The 2D correlation spectra include synchronous and asynchronous spectra. Each synchronous spectral peak located on the diagonal was designated as an "automatic peak" whose intensity reflects the sensitivity of the absorption peak to external interference. The denser the automatic peak profile, the stronger the peak and the more sensitive it is to external interference.

2.7.2. Spectra preprocessing

The center position and intensity of the 2D profile of the automatic peak in the synchronous spectrum were combined with the center position and intensity of the related 1D spectrum, and the characteristic spectral peaks sensitive to external interference were screened. Peaks located in non-diagonal positions were designated as "cross peaks," which reflect the relative strength of the change in vibration of pairs of groups at a given frequency. Positive cross peaks indicate that different components simultaneously increase or decrease under external interference. The more coordinated the intensity variation, the stronger the cross peak. In contrast, a negative cross peak represents a coordinated change in band intensity in the opposite direction. The 2D-COS analysis was performed using professional software (State Key Laboratory of Polymer Materials Engineering, Institute of Polymer Materials, Sichuan University).

2.7.3. CARS analysis

The results obtained using the CARS algorithm was compared to those obtained using 2D-COS. The CARS algorithm first eliminated variables (wavelengths) without any dominant features of "survival-of-the-fittest" and later discarded too many variables; therefore, insufficient information was retained for subsequent models (Yuan et al., 2020).

2.8. Model establishment and evaluation

Two typical methods (PLSR and LS-SVM) were applied to establish models between the spectral data and chemical compositions, respectively. PLSR is considered an advanced form of multiple and linear regression models (such as general stepwise regression) that combines the advantages of principal component analysis, canonical correlations, and multiple linear-regression analysis (Saeed et al., 2021) and is used to identify fundamental relationships between two matrices (X and Y).

LS-SVM is considered a modified version of SVM with strong generalization capability, low computing complexity, and a high solving speed (Yousefi et al., 2021). The distribution of the training data in the feature space depends on the choice of kernel function used to map the nonlinear input space. The radial basis function (RBF) kernel is frequently used in regression models owing to its influence and speed during training. The RBF kernel was calculated as follows:

$$K(x, x_i) = e^{(-\|x-x_i\|/2\sigma^2)}$$

where σ is the kernel width (used to adjust the degree of generalization), x_i is the input vector, and y_i is the corresponding output vector. In addition, the σ^2 must be optimized to create an LS-SVM model with an RBF kernel.

All datasets were partitioned into calibration and prediction sets using the Kennard–Stone algorithm, at a 3:1 ratio. Thus, 112 samples were used for modeling, and the remaining 37 samples were used for model validation. The model goodness was evaluated using the correlation coefficients of calibration (R_c) and verification (R_v), the root mean square error of calibration (RMSEC) and verification (RMSEV), and the residual predictive deviation (RPD). In general, a good model should have a high R value and a low RMSE value. An RPD value of <1.5 indicates a poor model. When the RPD is between 1.5 and 2.5 and R is between 0.8 and 0.9, the model should be suitable for rough predictions (Malley et al., 2005). When the RPD is between 2.5 and 3.0 and R is between 0.9 and 1.0, the model should perform well and be suitable for quantitative sample analysis.

2.9. Visualization of the indicators in potato tubers

In this study, the optimum regression model was used to transform the hyperspectral data from the samples into chemical images and represent the content distributions of the potato tubers by inputting each pixel's spectrum into an established calibration model. Finally, the visual distribution maps were illustrated using a linear color scale, signifying the corresponding values of the predicted contents of interest in the potato tubers. All procedures implemented for the HSI data analyses and the algorithm implement were performed using MATLAB software.

3. Results

3.1. Analysis of dry rot potato

Fig. 2 shows healthy potatoes and potatoes with different degrees of disease. The surfaces of the diseased tubers did not differ from those of the healthy tubers, and no obvious symptoms were discernable in the early stage. Subsequently, the pathogen enters host cells, releases specific toxins that destroy the defense system, and disrupts the normal physiological activities of the host, which causes changes in the contents of carbohydrates such as tuber starch, amylose, amylopectin, reducing sugar, sucrose, and total soluble sugar and affects the quality attributes of potatoes. Brown dots can be observed on the surfaces and insides of tubers; these dots are either soaked or wrinkled. Over time, pathological changes in potato tubers cause them to expand gradually and became dry and hollow. The potato skin folds into concentric circles, and the mycelium diffuses from the rotting part to produce white spore clusters. The diseased potato flesh is necrotic and brown, and its spreads in all directions. Fungal spores grow in necrotic tissue, and hyphae fill cavities. Table 2 shows basic statistics for potatoes with different degrees of disease. The spotted areas ranged from 0.22 to 15.40 cm^2 in size, accounting for 0.14 to 10.20% of the total potato surface area.

3.2. Statistical analysis of the reference values

As shown in Table 3, the range of reference values for the starch, soluble protein, and MDA contents and the total colonies were 11.40%-19.70%, 13.32–28.79 mg/g FW, 6.20–20.13 nmol/g FW, and 3.51–6.48 log10 CFUs/g, respectively. The mean values were 16.35%, 20.04 mg/g FW, 11.98 nmol/g FW, and 4.86 log10 CFUs/g, and the associated standard deviations were 0.019%, 3.74 mg/g FW, 2.89 nmol/g FW, and 0.73 log10 CFUs/g, respectively.

Fig. 3 (A) shows the variations in starch and soluble proteins observed with increasing degrees of corruption. In our study, the starch content was estimated to be 19.10%. The starch content decreased sharply on day 3 after pathogen inoculation, which led to rapid

Table 2
Statistics for spot areas of potatoes with different degrees of dry rot disease.

Degree	Area size range of disease spot (cm^2)	Average value (cm^2)	Standard deviation	Percentage of diseased spot area (%)
0	–	–	–	–
1	–	–	–	–
2	0.22–7.36	2.36	1.81	0.14–4.88
3	8.16–15.40	10.66	2.16	5.40–10.20

Table 3
Contents of components in potatoes with different degrees of dry rot disease.

Components	Contents			
	Healthy	D 1	D 2	D 3
Starch (%)	18.50–19.70	18.00–19.40	12.60–18.20	11.40–13.50
Soluble protein (mg/g FW)	13.35–15.19	15.01–17.54	13.32–26.26	25.61–28.79
MDA (nmol/g FW)	6.20–8.19	8.07–10.79	10.30–16.68	16.37–20.13
Aerobic bacterial count (log$_{10}$ CFUs/g)	3.51–3.83	3.95–4.63	4.67–5.90	5.92–6.48

pathogen infection, cell wall damage, and a subsequent gentle decrease in starch content as the degree of corruption increased. The reduction in starch content reached 12.25% by day 21. The decrease in starch content might be due to the phytopathogen infestation, which leads to an increase in hydrolytic enzymes such as amylases (Wei et al., 2022). Another reason may be that the reduction in starch content reflects nutrient decomposition and consumption by *Fusarium* during active infection, which enables fungal growth and reproduction. The results of this study are consistent with those reported in the literature (Tiwari et al., 2021).

As the main components of the plant body, proteins in the plant body have a corresponding influence after being infected with pathogenic bacteria. The soluble protein content of potato tubers increased after *Fusarium* infection over the entire period (Fig. 3A). The results of the present study show that the protein content of plants often increases after infection by pathogens, which may be mainly because the infection of pathogens promotes the initiation of the plant's defense response. Simultaneously, the corresponding changes in the cell led to the acceleration of cell division, increased synthesis of resistant substances, and increased resistance to further infection by pathogenic bacteria (Wang et al., 2023). Soluble proteins are an important aspect of the nutritional quality of edible potatoes and play a protective role in cell viability and
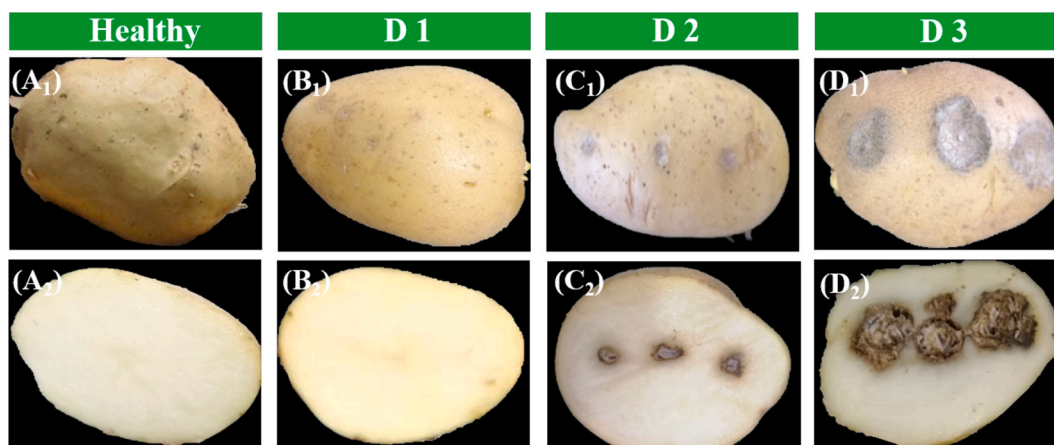

Fig. 2. The schematic diagram of potatoes with different degrees of disease.
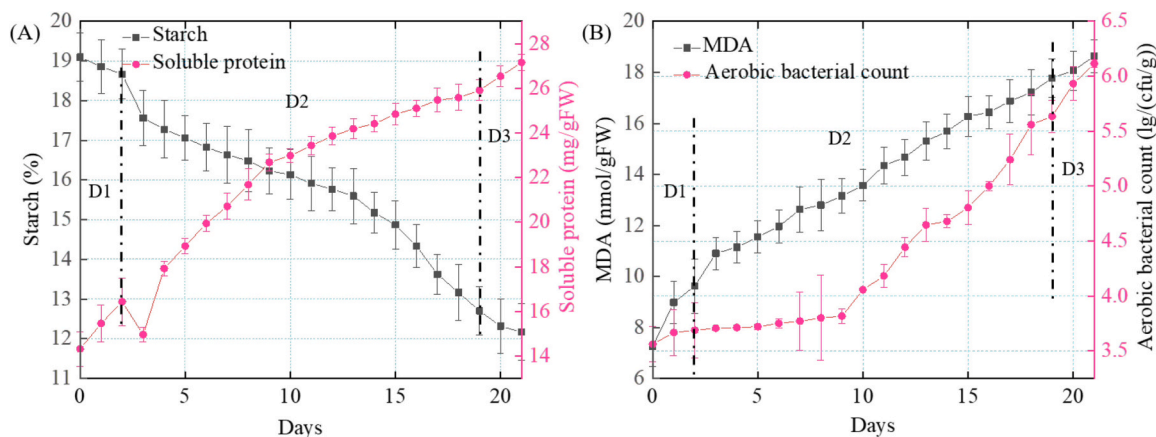
Fig. 3. The variations of starch, soluble proteins, MDA, and aerobic bacterial counts with increasing degrees of corruption.

biofilm formation. An increase in the soluble protein content in potato tubers is an important mechanism for resisting *F. sambucinum* infection (Jain et al., 2022). Additionally, soluble protein content decreased sharply on the third day after infection. At this time, the pathogenic bacteria reproduce by synthesizing their own proteins using the host's nitrogen-containing compounds, the plant proteins degrade to a certain extent, and the total nitrogen and protein contents decrease.

Potato tubers were infected with *F. sambucinum*, and changes in MDA content are shown in Fig. 3 (B). The MDA content gradually increased with an increasing degree of corruption. On the third day after pathogen inoculation, the MDA levels sharply increased, indicating that the rapid invasion of *Fusarium* caused the destruction of cell membranes (resulting in membrane oxidation) and eventually produced more MDA. The sustained increase showed that infection with pathogenic bacteria sustained damage to the structure of the cell membrane, causing continuous peroxidation of lipids on the surface of the membrane and resulting in considerable oxidative stress. Increased levels of oxidative stress have also been observed in bitter gourd fruit (Dolatmand-Shahri et al., 2024). Moreover, the change in MDA content showed the same trend when Korla fragrant pears were infected with smut (Yang et al., 2024).

Fig. 3B shows the changes in the aerobic bacterial counts as the degree of corruption increased. The aerobic bacterial counts increased during the entire infection period. This phenomenon is mainly due to infection with the *Fusarium* fungus, which increases the susceptibility of potato cells to secondary bacterial infections. The dotted line in Fig. 3 divides the content of the four components into three ranges: D 1, D 2, and D 3. Table 2 shows the range of potato content with different degrees of corruption.

3.3. Spectral characteristics

The presence of background noise tends to reduce differences between target and background spectra, resulting in a low signal-to-noise (SNR) ratio for a given band. Therefore, we removed information with a low SNR at the end of the original spectra, and only data within the range of 920 to 2086 nm (209 bands) were retained for subsequent analysis. The original spectra curves in the ROIs of all samples are shown in Fig. 4A. The spectra of healthy potatoes and potatoes with different degrees of corruption showed consistent trends; however, some differences occurred in the spectral-reflectance intensities at different wavelengths, indicating that different samples contained similar substances but at different concentrations (Li et al., 2021). The spectral region contained several valleys and peaks, attributed to chemical group molecular vibration (Xie et al., 2024). The strongest local absorption peaks were identified at 1005, 1223, and 1582 nm, which were ascribed to the presence of the second octaves of C—H and the first octave of stretching vibration absorption of N—H bonds in proteins (Zhang et al., 2024). A spectral-reflectance valley occurred 1360 nm, which was ascribed to the presence of O—H bonds in water in the second octaves (Li et al., 2022).

To further explore the infection trend of dry rot disease, a hyperspectral dataset after classification was arranged to reflect the changing trend of the infection degree of the potato samples. The average absorbance spectra of 23 grade-0 samples, 18 grade-1 samples, 91 grade-2 samples, and 17 grade-3 samples were plotted (Fig. 4B). Potatoes with dry rot and healthy potatoes showed clear differences in terms of their average spectra. Overall, potatoes with dry rot showed significantly higher average absorbance spectra than healthy potatoes. However, the
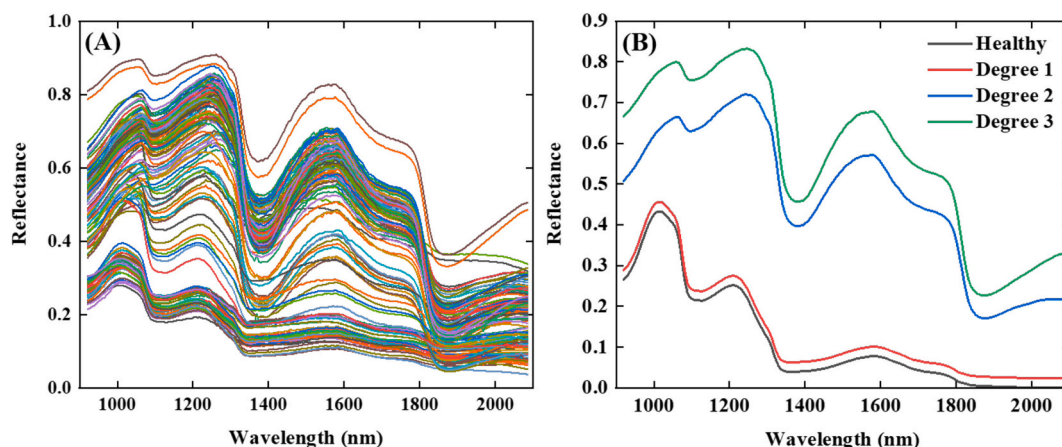

Fig. 4. Trend chart of index content change.

mean spectra of healthy and gleyic potato samples were similar, which may be due to the fact that the main physiological and biochemical indexes of most potato samples at the early stage of infection with pathogenic bacteria were not significantly changed. In contrast to healthy potatoes, potatoes with dry rot turn black and their tissues lose water. Potatoes with moderate or severe dry rot disease may consist of floury cortical tissues. During reflection, potato discoloration increases the light absorbed by the tissue, and tissue water loss may lead to enhanced light scattering by the tissue, which increases the absorbance (Zhang et al., 2024).

3.4. Modeling based on the full bands

In this study, SNV, FD, SD, SNV-FD, SNV-SD, FD-SNV, and SD-SNV were used to preprocess the original data, and the LS-SVM and PLSR models were subsequently established. Table 4 shows the predictive performance of the various LS-SVM models built using the full spectra with different pretreatment steps, where bold represents the best pretreatment model. After pretreatment, starch, soluble proteins, MDA, and aerobic bacterial counts improved. This shows improved accuracy and robustness compared with the original spectral results. Moreover, the SNV-FD, SD, FD-SNV, and SD-SNV methods were the best pretreatment methods for the starch, soluble protein, MDA, and aerobic bacterial count models, with R_v and RPD values of 0.8984 and 2.0368, 0.9056 and 1.8392, 0.9100 and 3.0229, and 0.9299 and 2.3328, respectively. Generally, scatter correction using SNV and their derivatives has successfully minimized overlapping peaks and corrected the baseline shift (Dharma et al., 2018).

The results of the PLSR models built with full spectra for the four indicators are shown in Table 5, and the PLSR model was established based on different pretreatments. The bold represents the best pretreatment model. The best pretreatments were SNV-FD, FD-SNV, FD, and FD for starch, MDA, soluble protein, and aerobic bacterial counts, respectively. The R_v values of the models built using data for starch,

soluble protein, MDA, and aerobic bacterial counts were 0.9068, 0.8836, 0.8812, and 0.9042, respectively, and the RPD values were 2.2095, 2.0591, 2.7590, and 2.2165, respectively. The LSSVM model outperformed the PLS model for all quality indicators, possibly because the PLS model only accounts for the linear relationship between spectral data and metrics, whereas the LSSVM model considers all useful linear and potentially nonlinear information (Walsh et al., 2020). These results are consistent with those of previous studies (Bao et al., 2014; Li et al., 2023).

3.5. Modeling based on feature bands

Redundant spectral curve information is not conducive for constructing models. Therefore, characteristic wavelengths should be extracted before inputting the data into a model to reduce the model input vectors and avoid introducing incorrect information into the established model.

3.5.1. Selection of characteristic wavelengths by 2D-COS

As shown in Fig. 5A, the days of culture were taken as external interference, and the mean spectra of samples from 0 to 21 d post-inoculation were selected for one strip each. All spectra were pretreated with S-G smoothing and FD analysis. Then, bands showing large spectral differences with samples at different days post-inoculation were selected to obtain two-dimensional correlation synchronization spectra and autocorrelation spectra for those bands.

As shown in Fig. 5B, the spectra could be divided into eight sub-bands, which were analyzed by 2D-COS. Fig. 5C2-J2 show the synchronous two-dimensional correlation spectra of the indicated bands and their corresponding autocorrelation spectra, respectively. The overlapping peaks in the conventional spectra became clearer when the characteristic bands were studied. According to Noda's theory of two-dimensional spectra, synchronous two-dimensional correlation spectra are symmetric along the main diagonal, and the correlation peak may

Table 4
Comparison of the results of the LS-SVM models built by full spectra with different pretreatments.

Indicator	Pretreatment method	R_c	R_v	RMSEC	RMSEP	RPD
	SNV	0.9536	0.7827	0.0060	0.0125	1.3365
	FD	0.8894	0.8009	0.0091	0.0110	1.1236
	SD	0.9889	0.8424	0.0030	0.0097	1.7568
Starch	SNV-FD	0.9750	0.8984	0.0043	0.0088	2.0368
	SNV-SD	0.9780	0.8512	0.0041	0.0103	1.6392
	FD-SNV	0.9582	0.8797	0.0055	0.0097	1.7061
	SD-SNV	0.9853	0.9028	0.0032	0.0094	1.9105
	SNV	0.9042	0.8718	1.1720	1.3197	1.6181
	FD	0.8906	0.8307	1.2106	1.6698	2.1786
	SD	0.9946	0.8218	0.2929	1.5237	1.6796
MDA	SNV-FD	0.9648	0.8560	1.1570	1.7270	1.7184
	SNV-SD	0.9887	0.8157	0.4194	1.3955	1.3955
	FD-SNV	0.9502	0.9299	0.7961	1.3023	2.3328
	SD-SNV	0.9936	0.8489	0.3279	1.4476	2.0038
	SNV	0.9026	0.7826	1.6876	2.1138	1.3919
	FD	0.9197	0.8326	1.4168	2.5699	1.2638
	SD	0.9623	0.9056	1.1248	1.5590	1.8392
Soluble protein	SNV-FD	0.9703	0.8565	0.9308	2.9141	1.7423
	SNV-SD	0.9743	0.8428	0.7922	1.9854	1.4650
	FD-SNV	0.9611	0.8395	1.0571	2.2086	1.7110
	SD-SNV	0.9532	0.8406	1.2288	1.7339	1.3414
	SNV	0.9201	0.8666	0.2854	0.3452	1.8114
	FD	0.9390	0.8540	0.2526	0.3548	1.7640
	SD	0.9713	0.8352	0.1680	1.55	1.84
Aerobic bacterial count	SNV-FD	0.9594	0.8513	0.1988	0.4132	1.4698
	SNV-SD	0.8995	0.8060	0.3318	0.3860	1.6045
	FD-SNV	0.9813	0.8081	0.1680	0.4222	1.3769
	SD-SNV	0.9744	0.9100	0.2048	0.3017	3.0229

Table 5
Comparison of the results of the PLSR models built by full spectra with different pretreatments.

Indicator	Pretreatment method	R_c	R_v	RMSEC	RMSEP	RPD
Starch	SNV	0.8839	0.8770	0.0155	0.0098	1.9675
	FD	0.8551	0.8456	0.0098	0.0108	1.7183
	SD	0.8983	0.8552	0.0085	0.0104	1.7799
	SNV-FD	0.9207	0.9068	0.0073	0.0088	2.2095
	SNV-SD	0.8963	0.8053	0.0083	0.0095	1.9775
	FD-SNV	0.9207	0.9056	0.0075	0.0090	2.1984
	SD-SNV	0.9080	0.8814	0.0078	0.0097	1.9995
MDA	SNV	0.8947	0.8746	1.2178	1.3335	1.8825
	FD	0.8998	0.8673	1.1906	1.9212	1.9212
	SD	0.8931	0.8687	1.2283	1.3608	1.8049
	SNV-FD	0.9082	0.8667	1.1409	1.3681	1.7958
	SNV-SD	0.8988	0.8917	1.2167	1.1801	2.0921
	FD-SNV	0.9079	0.8812	1.1084	1.4424	2.7590
	SD-SNV	0.9078	0.8696	1.1638	1.3796	2.0057
Soluble protein	SNV	0.8763	0.8310	1.8119	2.1251	1.6375
	FD	0.9081	0.8836	1.5753	1.8065	2.0591
	SD	0.8860	0.8521	1.7550	1.9388	1.6214
	SNV-FD	0.8858	0.8289	1.7452	2.1447	1.6394
	SNV-SD	0.8870	0.8717	1.7041	1.9797	1.8984
	FD-SNV	0.8940	0.8396	1.6849	2.0740	1.6871
	SD-SNV	0.8903	0.8861	1.6805	1.8602	1.9966
Total colonies	SNV	0.9291	0.9046	0.2605	0.3336	2.1547
	FD	0.9284	0.9042	0.2619	0.3553	2.2165
	SD	0.9060	0.8780	0.3004	0.3473	1.9833
	SNV-FD	0.9377	0.9001	0.2448	0.3515	2.1488
	SNV-SD	0.8674	0.7861	0.3816	0.4549	1.4585
	FD-SNV	0.9412	0.9006	0.2380	0.3495	2.1232
	SD-SNV	0.8519	0.8188	0.3989	0.4176	1.5198

appear on or off the diagonal (An et al., 2024). The peak on the diagonal is called the automatic peak, which is always positive, and its strength reflects the change in intensity of the system when tested with an external disturbance. The number of circles reflects the strength of the automatic peak. By studying the two-dimensional correlation spectral characteristics of potatoes, we were able to select 20 autocorrelation peaks as characteristic wavelengths, which were 960, 1005, 1083, 1089, 1134, 1139, 1274, 1307, 1347, 1498, 1531, 1587, 1632, 1677, 1716, 1789, 1845, 1946, 2019, and 2064 nm.

All the selected wavelengths belonged to the VNIR/SWIR region of the spectra and were related to the vibration and combination overtones of the C—H, O—H, and N—H bonds, which are the primary structural components of organic molecules. Like all fresh fruits, potatoes are mainly composed of water, with the second major component being carbohydrates. Due to this, strong carbohydrate absorbance bands exist at 1134 and 1139 nm. The water absorption peaks are observed at 960 nm (third overtone of O—H stretching vibration), 1498 nm (O—H stretch first overtone), and 1946 nm (O—H stretch and O—H deformation) (Williams & Norris, 1987). The peak at 1845 nm was associated with the O—H stretching vibration of sugar (Baiano et al., 2012). Strong autocorrelation peaks appeared at 1083 and 1089 nm that were related to the second-frequency stretching vibrations of the C—H bonds. The peak at approximately 1274 nm is due to the absorption band of the C—H stretching second overtone, which is related to anthocyanin compounds (Chen et al., 2015). The peaks at 2019 and 2064 nm are related to combinations of aromatic C—H and C=C stretching vibrations, respectively. The results show that the 2D-COS algorithm can effectively extract the characteristic wavelengths related to the internal properties of dry-rot potatoes.

3.5.2. Selection of characteristic wavelengths using the CARS algorithm

The CARS algorithm was used to screen for characteristic wavelengths after spectral preprocessing. The number of Monte Carlo samples was set to 1000, and the number of selected wavelengths was

determined using the 10-fold cross validation method. Fig. S1 shows the CARS wavelength-selection procedure and characteristic wavelengths. Fig. S1A-F presents the starch, soluble protein, MDA and aerobic bacterial counts models of LS-SVM and PLSR.

Differences in the sample variables were divided into two stages. The first stage (rapid selection) decreased rapidly, and the second (refined selection) decreased extremely slowly. When the sampling times were 1–600, 1–21, 1–620, 1–23, 1–603, and 1–605, the cross-validation root mean square error (RMSECV) value continued to decrease, indicating that variables unrelated to fungal contamination were eliminated during the selection process. In contrast, when the number of sampling points reached 600, 21, 620, 23, 603, and 605, the RMSECV showed an upward trend, indicating that key variables may have been eliminated. Fig. S1A3-F3 present changes in the regression coefficients of all variables during each sampling process. We found that when sampling was conducted 530, 21, 440, 10, 389, and 480 times, the RMSECV value was the smallest, meaning that the subset of selected spectral variables was optimal. After running the CARS algorithm, the subset contained 16, 18, 22, 31, 36, and 24 spectral variables (Fig. S1A4-F4). Compared with the original variables, these values were 92.34%, 91.39%, 89.47%, 85.17%, 82.78%, and 88.52% lower, respectively. This shows that the CARS algorithm can effectively reduce the number of wavelengths.

3.6. Analysis of the modeling results

Spectra pretreated using the SNV-FD, FD-SNV, SD, and SD-SNV methods at characteristic wavelengths were treated as independent variables, and the measured starch, soluble protein, MDA, and aerobic bacterial counts were treated as dependent variables to further simplify the LS-SVM and PLSR models. Fig. 6 shows the results of the LS-SVM and PLSR models with full and characteristic wavelengths generated by the 2D-COS and CARS analyses for the four indicators. The model with the screened characteristic wavelengths generated better predictions than the full-wavelength models because of the selection of valid variables,
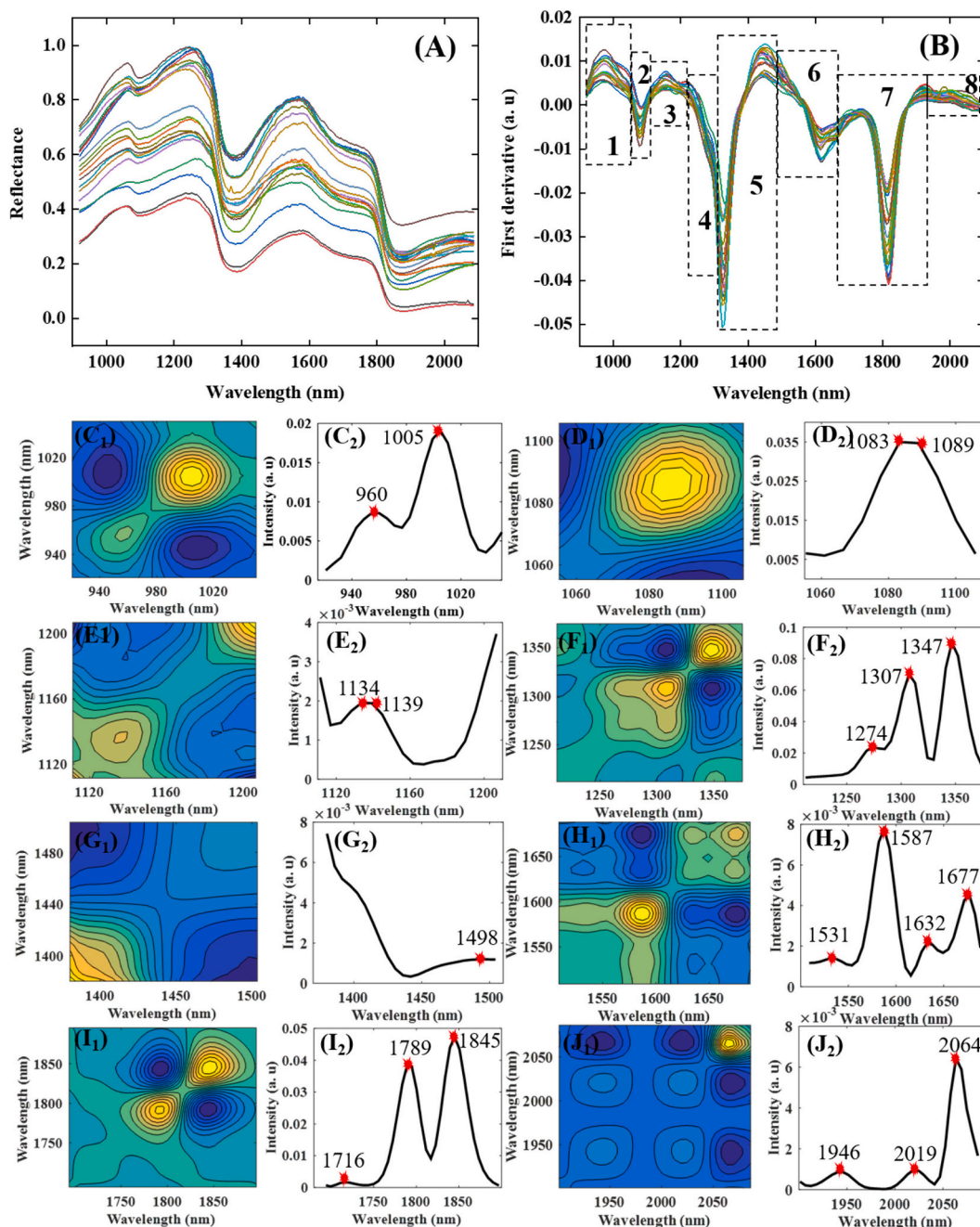
Fig. 5. The result of models based on the characteristics after pretreatments.

which improved model accuracy. The R_v values of the best models were 0.9273, 0.9634, 0.9470, and 0.9487, and the RPD values were 2.5506, 3.7201, 2.7517, and 2.8896 for starch, soluble protein, MDA, and aerobic bacterial count, respectively. Compared with the CARS algorithm, the models based on 2D-COS exhibited better performance. This may be because 2D-COS is implemented by selecting an intrinsic relationship between the variables associated with external perturbations and target class classification. The improved modeling performance indicates that the model can be effectively simplified, and its prediction ability can be improved by eliminating irrelevant variables.

3.7. Visualization

The above results indicate that HSI combined with LS-SVM could be used as an effective tool for rapidly and non-destructively evaluating the indicators of interest in potato samples. For hyperspectral images, a combination of smoothing, derivative, and SNV methods was used to preprocess the pixel-wise spectra in the ROI and input the data into the 2D-COS-LSSVM model to visually demonstrate the content distribution of the four indicators. Pixel-wise prediction maps were beneficial for understanding compositional distributions in potato tubers. Fig. 7 illustrates some distribution maps related to changes in the starch, soluble protein, MDA, and aerobic bacterial counts. The average reference values are shown underneath the images. The linear color bar on the right indicates different concentrations, ranging from blue and red, which represent low to high values for each parameter.

Vertical stripes were observed in each distribution map, possibly because of random vibrations occurring during spectral push broom scanning. In addition, the starch, soluble protein, and MDA densities were nonuniform, irregular, and mainly distributed at irregular margins,
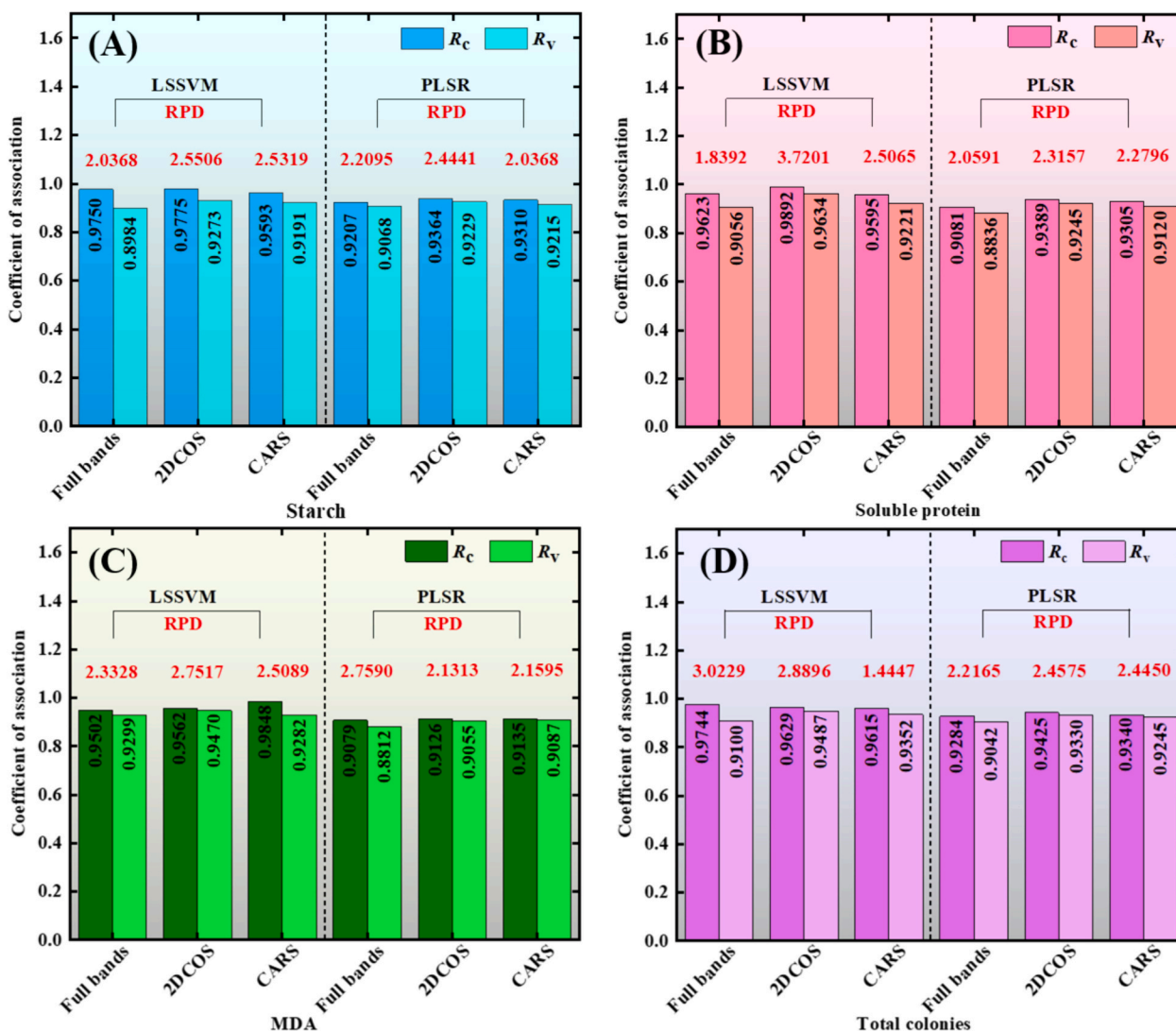
Fig. 6. The results of the LS-SVM and PLSR model with full and characteristic wavelengths by 2DCOS, CARS for four indicators.

which may be attributed to complex biochemical changes (e.g., protein decomposition and moisture loss). As shown in Fig. 7, the variations in the starch contents ranged from 12.2 to 19.10%. With increasing starch contents, the color of the corresponding distribution map gradually faded from red to blue. The image of a corrupt sample shows that the starch content in the corrupted area was minor. The color of the corresponding distribution map gradually changed from blue to red with increasing soluble protein contents, MDA contents, and aerobic bacterial counts. Specifically, the highest content values were identified in corrupt areas. Therefore, object-wise prediction maps could be used to non-destructively visualize the starch, soluble protein, and MDA contents, as well as the aerobic bacterial counts in individual potato tubers.

4. Discussion

In this study, we used HSI to detect potato dry rot disease and measured the physical and chemical changes in the samples during infection. Starch is an important constituent of carbohydrates present in potatoes, which provide metabolic energy that enables the body to perform its function. The starch content of potatoes is affected by storage, repair, abiotic stress, and biological stress (Lal, Tiwari, et al., 2021). We found that pathogenic bacteria may decompose and consume cellular nutrients in potato tubers during potato tuber infection, which lowers starch content. It has been previously reported that biotic stresses

such as viral infection have detrimental effects on starch quality-related parameters. Lal et al. reported that the apical leaf curl disease infection in Kufri Pukhraj potatoes caused a severe reduction in starch content during storage (Lal, Singh, et al., 2021). Additionally, it was previously recorded that *F. sambucinum* and *F. oxysporum* infections led to a substantial reduction in starch content in Kufri Pukhraj and Kufri Chipsona varieties (Tiwari et al., 2021). The findings of this study are in agreement with previous reports on the correlation between amylose reduction and fungal infection in potato tubers.

We found that soluble protein content increased with an increasing degree of dry rot, which may reflect a stress response to infection with exogenous pathogenic bacteria that are closely related to the activation of various defense enzymes in potato tubers. It has also been reported that the reason for the increase in protein content of infected plants may be that after the occurrence of pathogenic fungal infection, the activity of plant protein synthetase increases or inhibits the activity of protein-degrading enzyme, resulting in an increase in protein content, and at the same time promotes the synthesis of proteins that are different from normal tissues, that is, "disease-course related proteins," such as ribosome inactivated proteins and penetrant proteins (Jain et al., 2022).

MDA is toxic to plant cells, causing cell membrane dysfunction and the destruction of many functional molecules. Therefore, increased MDA content can directly damage plant cells. Previous studies have found that banana infection with *Fusarium oxysporum* f. sp. *cubense* can lead to
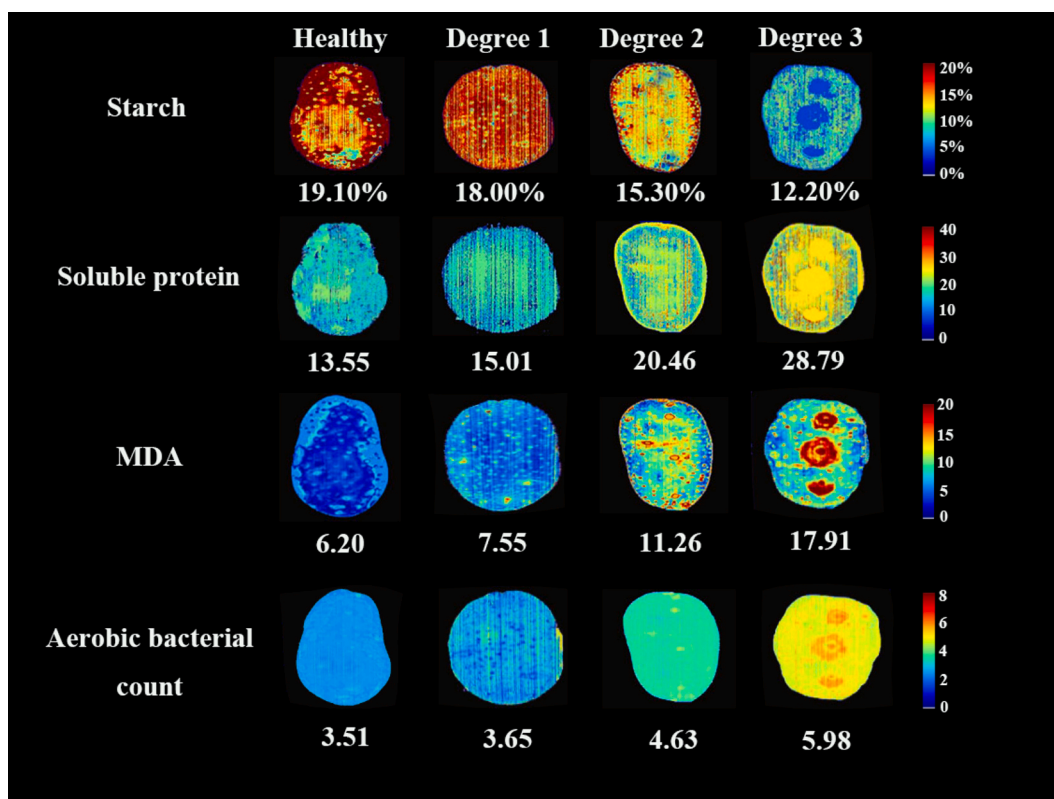
Fig. 7. The distribution maps related to changes in the starch, soluble protein, MDA, and aerobic bacterial counts.

increased MDA levels and that the degree of infection is positively correlated with MDA accumulation (Sun et al., 2013). A similar phenomenon was also found in the pathogenesis of ring rot in crown pears, resulting in the rapid accumulation of malondialdehyde. These studies indicate that MDA accumulation is not conducive to fruit disease resistance (Sun et al., 2017), which is consistent with our findings. When the degree of potato dry rot disease increased, the aerobic bacterial counts consistently increased with a relatively stable trend, mainly because of infection with the *Fusarium* fungus, which increased the susceptibility of potato cells to secondary bacterial infections.

Changes in the internal components mentioned above inevitably lead to changes in the optical properties of the potatoes. Therefore, models were established for the four physicochemical indices and spectral variables. First, different pretreatments were used to pretreat the entire spectra, and PLSR and LS-SVM models were established. The results showed that the SNV-FD, SD, FD-SNV, and SD-SNV methods were the best pretreatment methods for all four indicators. The best pretreatment methods differed in the prediction of different indicators. This result is consistent with that reported in the literature (Zhang et al., 2022). In addition, the LS-SVM model performed better than the PLSR model, primarily because the LS-SVM algorithm considers all useful linear and potentially nonlinear information. We obtained the same results as in Yin et al. (2023). The RMSE values were slightly larger for both the original and preprocessed spectra, indicating that the model was general and could not accurately characterize the degree of dry rot.

To further verify the advantages of hyperspectral data combined with 2D-COS analysis of quantitative peaks, quantitative peaks were used to establish a prediction model and compared with the results of the CARS model. The results demonstrated that both the CARS and 2D-COS methods improved the predictive capability of the model; however, the model built using the 2D-COS filtering variables was more accurate, indicating that the combined model with 2D-COS screened the characteristic wavelengths more effectively. The identified automatic peaks revealed a self-correlation of functional groups that were sensitive to

fungal infection in dry-rot potatoes. By combining this with asynchronous spectra, sensitive functional groups related to fungal infection and their changing orders can be determined.

A unique advantage of HSI technology compared with traditional spectroscopy or computer imaging technology is visualization of the prediction index of tested samples. Therefore, HSI containing potatoes were respectively input to the calibrated 2DCOS-LSSVM model to obtain the predicted starch, soluble protein, and MDA value of each pixel, and pseudo-color was used to display the contents distribution of each individual potato. Similar works for internal attribute were investigated by Wang et al., 2024 and Xu et al., 2022. According to the distribution maps for different components, rapidly and nondestructively evaluating the potato quality is beneficial for both consumers and industries. Our findings provide clear evidence that HSI is more powerful than NIR. These findings not only provide a theoretical basis for predicting the values of different physical and chemical indexes but also provide a novel approach for screening characteristic variables during near-infrared (NIR) spectrum analysis.

5. Conclusions

This study demonstrated the effectiveness of HSI and 2D-COS in detecting starch, soluble protein, MDA content, and aerobic bacterial counts in dry rot potatoes. The feasibility of the 2D-COS algorithm in extracting the characteristic information of the spectra was proven, and the extracted feature information was closely related to the internal attributes, which significantly improved the model performance. The best prediction results for the four indicators were obtained from spectra selected using the 2D-COS algorithm. The R_v values of these quantitative models were 0.9273, 0.9634, 0.9470, and 0.9487, and the RPD values were 2.5506, 3.7201, 2.7517, and 2.8896, respectively. Additionally, visual analysis revealed the content distribution of the four indicators in the potatoes. In conclusion, this study demonstrates the potential of the HSI technique combined with the 2D-COS algorithm for practical

applications in detecting starch, soluble protein, MDA content, and aerobic bacterial counts of potato samples to identify the early stages of potato dry rot. Based on the proposed algorithm, further investigations are required to realize the early detection of other plant diseases.

CRediT authorship contribution statement

Fan Zhang: Writing – original draft, Data curation. **Wenxiu Wang:** Funding acquisition, Formal analysis. **Qianyun Ma:** Software, Investigation. **Qi Shi:** Validation, Supervision. **Kexiang Chen:** Visualization. **Xinyue Pan:** Formal analysis. **Shiyuan Xie:** Validation. **Jianfeng Sun:** Writing – review & editing.

Declaration of competing interest

The authors declare that they have no known competing financial interests or personal relationships that could have appeared to influence the work reported in this paper.

Data availability

The authors do not have permission to share data.

Acknowledgments

Appendix A. Supplementary data

Supplementary data to this article can be found online at https://doi.org/10.1016/j.fochx.2024.101574.

References

An, H. J., et al. (2024). Insight into microstructure evolution during starch retrogradation by infrared and Raman spectroscopy combined with two-dimensional correlation spectroscopy analysis. *Food Hydrocolloids, 146*, Article 109174. https://doi.org/10.1016/j.foodhyd.2023.109174

Baiano, A., Terracone, C., Peri, G., & Romaniello, R. (2012). Application of hyperspectral imaging for prediction of physico-chemical and sensory characteristics of table grapes. *Computers and Electronics in Agriculture, 87*, 142–151. https://doi.org/10.1016/j.compag.2012.06.002

Bao, Y. D., Liu, F., Kong, W. W., Sun, D. W., He, Y., & Qiu, Z. J. (2014). Measurement of soluble solid contents and pH of white vinegars using VIS/NIR spectroscopy and least squares support vector machine. *Food and Bioprocess Technology, 7*, 54–61. https://doi.org/10.1007/s11947-013-1065-0

Bian, X. H., Wang, K. Y., Tan, E. X., Di-Wu, P. Y., Zhang, F., & Guo, Y. G. (2020). A selective ensemble preprocessing strategy for near-infrared spectral quantitative analysis of complex samples. *Chemometrics and Intelligent Laboratory Systems, 197*, Article 103916. https://doi.org/10.1016/j.chemolab.2019.103916

Chen, S., Zhang, F., Ning, J., Liu, X., Zhang, Z., & Yang, S. (2015). Predicting the anthocyanin content of wine grapes by NIR hyperspectral imaging. *Food Chemistry, 172*, 788–793. https://doi.org/10.1016/j.foodchem.2014.09.119

Dharma, S. D., Midi, H., Arasan, J., Shafie, M. M., & Caliman, J. P. (2018). Robust generalized multiplicative scatter correction algorithm on pretreatment of near infrared spectral data. *Vibrational Spectroscopy, 97*, 55–65. https://doi.org/10.1016/j.vibspec.2018.05.002

Ding, Y. G., Zhang, Q. Z., & Wang, Y. Z. (2021). A fast and effective way for authentication of Dendrobium species: 2D-COS combined with res net based on feature bands extracted by spectrum standard deviation. *Spectrochimica Acta. Part A, Molecular and Biomolecular Spectroscopy, 261*, Article 120070. https://doi.org/10.1016/j.saa.2021.120070

Dolatmand-Shahri, N., Dolatmand-Shahri, S. A. M., Mirjalili, M. H., & Mokhtassi-Bidgoli, A. (2024). Study the yield and quality of bitter gourd fruit (*Momordica charantia*) in inoculation with two species of mycorrhizal fungi and phosphorus fertilizer under different irrigation regimes. *Plant Physiology and Biochemistry, 208*, Article 108479. https://doi.org/10.1016/j.plaphy.2024.108479

Dong, J. E., Zhang, J., Zuo, Z. T., & Wang, Y. Z. (2021). Deep learning for species identification of bolete mushrooms with two-dimensional correlation spectral (2D-COS) images. *Spectrochimica Acta. Part A, Molecular and Biomolecular Spectroscopy, 249*, Article 119211. https://doi.org/10.1016/j.saa.2020.119211

Dong, J. E., Zuo, Z. T., Zhang, J., Zhong, Y., & Wang, Y. Z. (2021). Geographical discrimination of boletus edulis using two-dimensional correlation spectral or integrative two-dimensional correlation spectral image with ResNet. *Food Control, 129*, Article 108132. https://doi.org/10.1016/j.foodcont.2021.108132

Jain, M., Muluneh, G., Muthukumaran, J., & Singh, A. K. (2022). Insights into biological role of plant defense proteins: A review. *Biocatalysis and Agricultural Biotechnology, 40*, Article 102293. https://doi.org/10.1016/j.bcab.2022.102293

Lal, M. K., Singh, B., Sharma, S., Singh, M. P., & Kumar, A. (2021). Glycemic index of starchy crops and factors affecting its digestibility: A review. *Trends in Food Science & Technology, 111*, 741–755. https://doi.org/10.1016/j.tifs.2021.02.067

Lal, M. K., Tiwari, R. K., Kumar, R., Naga, K. C., Kumar, A., Singh, B., … Changan, S. S. (2021). Effect of potato apical leaf curl disease on glycemic index and resistant starch of potato (*Solanum tuberosum* L.) tubers. *Food Chemistry, 359*, Article 129939. https://doi.org/10.1016/j.foodchem.2021.129939

Li, D., Zhang, F., Yu, J., Chen, X., & Meng, X. (2021). A rapid and non-destructive detection of Escherichia coli on the surface of fresh-cut potato slices and application using hyperspectral imaging. *Postharvest Biology and Technology, 171*, Article 111352. https://doi.org/10.1016/j.postharvbio.2020.111352

Li, H. Q., Hong, S., & Li, M. Z. (2022). Study on identification of common diseases in potato storage period based on spectral structure. *Spectroscopy and Spectral Analysis, 42*(08), 2471–2476.

Li, L., Hu, D. Y., Tang, T. Y., & Tang, Y. L. (2023). Non-destructive detection of the quality attributes of fruits by visible-near infrared spectroscopy. *Journal of Food Measurement and Characterization, 17*, 1526–1534. https://doi.org/10.1007/s11694-022-01724-4

Macauley, B. J. (1982). Compendium of potato diseases. *Soil Biology & Biochemistry, 14*, 167–168. https://doi.org/10.1016/0038-0717(82)90064-5B

Malley, D. F., Mcclure, C., Martin, P. D., Buckley, K., & Mccaughey, W. P. (2005). Compositional analysis of cattle manure during composting using a field-portable near-infrared spectrometer. *Communications in Soil Science and Plant Analysis, 36*, 455–475. https://doi.org/10.1081/CSS-200043187

Ren, J., Tong, J., Li, P. H., Huang, X. Q., Dong, P., & Ren, M. Z. (2021). Chitosan is an effective inhibitor against potato dry rot caused by *fusarium oxysporum*. *Physiological and Molecular Plant Pathology, 113*, Article 101601. https://doi.org/10.1016/j.pmpp.2021.101601

Saeed, F., Khan, M. A., Sharif, M., Mittal, M., Goyal, L. M., & Roy, S. (2021). Deep neural network features fusion and selection based on PLS regression with an application for crops diseases classification. *Applied Soft Computing, 103*, Article 107164. https://doi.org/10.1016/j.asoc.2021.107164

Singh, P. P., & Saldaña, M. D. A. (2011). Subcritical water extraction of phenolic compounds from potato peel. *Food Research International, 44*, 2452–2458. https://doi.org/10.1016/j.foodres.2011.02.006

Sui, H. L., Liu, X. Y., Zhong, F. C., Cheng, K. M., Luo, Y. W., & Ju, X. (2014). Polyurethane thermal effects studied using two-dimensional correlation infrared spectroscopy. *Polymer Degradation and Stability, 110*, 13–22. https://doi.org/10.1016/j.polymdegradstab.2014.08.006

Sun, D., Lu, X., Hu, Y., Li, W., Hong, K., Mo, Y., Cahill, D. M., & Xie, J. (2013). Methyl jasmonate induced defense responses increase resistance to *fusarium oxysporum* f. sp. *cubense* race 4 in banana. *Scientia Horticulturae, 164*, 484–491. https://doi.org/10.1016/j.scienta.2013.10.011

Sun, P., Cui, J., Jia, X., & Wang, W. (2017). Isolation and characterization of *bacillus Amyloliquefaciens* L-1 for biocontrol of pear ring rot. *Horticultural Plant Journal, 3*, 183–189. https://doi.org/10.1016/j.hpj.2017.10.004

Tiwari, R. K., Bashyal, B. M., Shanmugam, V., Lal, M. K., Kumar, R., Sharma, S., … K., Singh, B., & Aggarwal, R.. (2021). Impact of *fusarium* dry rot on physicochemical attributes of potato tubers during postharvest storage. *Postharvest Biology and Technology, 181*, Article 111638. https://doi.org/10.1016/j.postharvbio.2021.111638

Veltman, B., Ma, J. N., Harpaz, D., Xing, F. G., & Eltzov, E. (2023). Genetically engineered bacterial strains constructed as a whole-cell biosensor for specific volatiles identification of infected potato tubers with a soft rot disease. *Sensors and Actuators B: Chemical, 387*, Article 133788. https://doi.org/10.1016/j.snb.2023.133788

Walsh, K. B., Blasco, J., Zude-Sasse, M., & Sun, X. D. (2020). Visible-NIR "point" spectroscopy in postharvest fruit and vegetable assessment: The science behind three decades of commercial use. *Postharvest Biology and Technology, 168*, 17. https://doi.org/10.1016/j.postharvbio.2020.111246

Wang, B. J., Shi, Y., Lu, H. Y., & Chen, & Q. H.. (2023). A critical review of fungal proteins: Emerging preparation technology, active efficacy and food application. *Trends in Food Science & Technology, 141*, Article 104178. https://doi.org/10.1016/j.tifs.2023.104178

Wang, Z. J., Ding, F. C., Ge, Y., Wang, M. Y., Zuo, C. Z., Song, J., … Pan, L. Q. (2024). Comparing visible and near infrared 'point' spectroscopy and hyperspectral imaging techniques to visualize the variability of apple firmness. *Spectrochimica Acta Part A: Molecular and Biomolecular Spectroscopy, 316*, Article 124344. https://doi.org/10.1016/j.saa.2024.124344

Wei, F. L., Ma, N. N., Haseeb, H. A., Gao, M. X., Liu, X. X., & Guo, W. (2022). Insights into structural and physicochemical properties of maize starch after fusarium verticillioides infection. *Journal of Food Composition and Analysis, 114*, Article 104819. https://doi.org/10.1016/j.jfca.2022.104819

Williams, P., & Norris, K. (1987). *Near-infrared Technology in the Agricultural and Food Industries*. American Association of Cereal Chemists, Inc.

Wood, K., & Carragher, J. (2017). Australian consumers' insights into potatoes - nutritional knowledge, perceptions and beliefs. *Appetite, 114*, 169–174. https://doi.org/10.1016/j.appet.2017.03.038

Wu, H. Y., Wei, Y., Yang, R. J., Jin, H., & Ai, C. L. (2020). Analysis of chalk in rice by two-dimensional correlation spectroscopy. *Journal of Molecular Structure, 1218*, Article 128471. https://doi.org/10.1016/j.molstruc.2020.128471

Xie, C. Q., Tang, W. S., Wang, C. Y., Zhang, Y. C., & Zhao, M. Y. (2024). Hyperspectral imaging for predicting and visualizing the acrylamide levels in roasted coffee. *Microchemical Journal*. https://doi.org/10.1016/j.microc.2024.110685

Xu, W., Zhang, F., Wang, J., Ma, Q., Sun, J., Tang, Y., Wang, J., & Wang, W. (2022). Real-time monitoring of the quality changes in shrimp (*Penaeus vannamei*) with hyperspectral imaging technology during hot air drying. *Foods, 11*, 3179. https://doi.org/10.3390/foods11203179

Yang, W. T., Sun, T. R., Sun, P. C., Tang, Y. S., Cheng, S. B., & Chen, G. G. (2024). Development of defense system and secondary metabolites of Korla fragrant pear during Alternaria alternata infection. *Postharvest Biology and Technology, 212*, Article 112865. https://doi.org/10.1016/j.postharvbio.2024.112865

Yin, H., Xie, B. H., Chen, B. J., Ma, J. F., Chen, J. Z., Zhou, Y. X., … Huang, F. R. (2023). Detection of moisture content and size of pumpkin seeds based on hyperspectral reflection and transmission imaging techniques. *Journal of Food Composition and Analysis, 124*, Article 105651. https://doi.org/10.1016/j.jfca.2023.105651

Yousefi, M., Gholami, M., Oskoei, V., Mohammadi, A. A., Baziar, M., & Esrafili, A. (2021). Comparison of LSSVM and RSM in simulating the removal of ciprofloxacin from aqueous solutions using magnetization of functionalized multi-walled carbon nanotubes: Process optimization using GA and RSM techniques. *Journal of Environmental Engineering, 9*, Article 105677. https://doi.org/10.1016/j.jece.2021.105677

Yuan, L. M., et al. (2020). Models fused with successive CARS-PLS for measurement of the soluble solids content of Chinese bayberry by vis-NIRS technology. *Postharvest Biology and Technology, 169*, Article 111308. https://doi.org/10.1016/j.postharvbio.2020.111308

Yun, Y. H., Li, H. D., Deng, B. C., & Cao, D. S. (2019). An overview of variable selection methods in multivariate analysis of near-infrared spectra. *Trac-Trends in Analytical Chemistry, 113*, 102–115.

Zhang, D. Y., Xu, Y. F., Huang, W. Q., Tan, X., Xia, Y., & Xu, L. (2019). Nondestructive measurement of soluble solids content in apple using near infrared hyperspectral imaging coupled with wavelength selection algorithm. *Infrared Physics & Technology, 98*, 297–304.

Zhang, F., Wang, W. X., Wang, C. S., Zhou, J., Pan, Y., & Sun, J. F. (2024). Study on hyperspectral detection of potato dry rot in gley stage based on convolutional neural network. *Spectroscopy and Spectral Analysis, 44*(2), 480–489.

Zhang, Y. F., Wang, W. X., Zhang, F., Ma, Q. Y., Gao, S., Wang, J., … Liu, Y. Y. (2022). Rapid and non-destructive decay detection of *Yali* pears using hyperspectral imaging coupled with 2D correlation spectroscopy. *International Journal of Agricultural and Biological Engineering, 15*, 236–244. https://doi.org/10.25165/j.ijabe.20221505.7313

Zhao, L., Zeng, Y., Liu, P., & Su, X. H. (2020). Band selection with the explanatory gradient saliency maps of convolutional neural networks. *IEEE Geoscience and Remote Sensing Letters, 17*, 2105–2109. https://doi.org/10.1109/LGRS.2020.3012140

Zheng, Y. J., Zhang, Y. T., Liu, H. C., Li, Y. M., Hao, Y. W., & Lei, B. F. (2018). Supplemental blue light increases growth and quality of greenhouse pak choi depending on cultivar and supplemental light intensity. *Journal of Integrative Agriculture, 17*, 2245–2256. https://doi.org/10.1016/S2095-3119(18)62064-7